

Manipulation of morphologies and magnetic properties for $\text{Bi}_{4.2}\text{K}_{0.8}\text{Fe}_2\text{O}_{9+\delta}$ nanostructures[†]

Cite this: *CrystEngComm*, 2013, **15**, 9057

Sining Dong, Yukuai Liu, Shengwei Yang, Tao Jiang, Yuewei Yin and Xiaoguang Li*

In this paper, $\text{Bi}_{4.2}\text{K}_{0.8}\text{Fe}_2\text{O}_{9+\delta}$ nanostructures with different morphologies, such as dispersible nanobelts, urchin-like and floriated micronanostructures with dendrites in different sizes, were controllably synthesized by a surfactant-free hydrothermal method. The temperatures of the KOH solutions in the co-precipitation step and the hydrothermal reactions had great effects on not only the morphologies but also the magnetic properties of the products. It was found that the low-temperature-fabricated urchin-like samples had a higher magnetization value. The special cores of the urchin-like nanostructures may play a critical role in the enhanced magnetizations and spin-glass dynamic behaviors. These results provide a simple way to manipulate the morphology of low-dimensional $\text{Bi}_{4.2}\text{K}_{0.8}\text{Fe}_2\text{O}_{9+\delta}$ nanostructures as well as their related magnetic properties.

Received 24th July 2013,
Accepted 19th September 2013

DOI: 10.1039/c3ce41464g

www.rsc.org/crystengcomm

1. Introduction

For the past decade, magnetoelectric multiferroic materials which have simultaneous ferroelectric and magnetic orders have drawn vast interest due to this novel physical phenomena as well as their potential applications in information storage, energy transformation and sensors.^{1–5} There is a bottleneck problem that only a few room-temperature single-phase multiferroics have been reported, such as BiFeO_3 ,⁶ $\text{Sr}_3\text{Co}_2\text{Fe}_{24}\text{O}_{41}$ ⁷ and so on. Recently, two new room-temperature multiferroic compounds, KBiFe_2O_5 and $\text{Bi}_{4.2}\text{K}_{0.8}\text{Fe}_2\text{O}_{9+\delta}$, have been fabricated *via* hydrothermal reactions, opening a special route to search for more multiferroic materials.^{8,9} The basic structure of $\text{Bi}_{4.2}\text{K}_{0.8}\text{Fe}_2\text{O}_{9+\delta}$ (BKFO) is similar to that of the high temperature superconductor $\text{Bi}_2\text{Sr}_2\text{CaCu}_2\text{O}_{8+\delta}$ (Bi2212),¹⁰ and the major differences between them are the distinct perovskite units sandwiched between the rock salt slabs. The CuO planes in the perovskite blocks of Bi2212 are critical to the superconductivity while the BiFeO_3 -like perovskite blocks in BKFO can be regarded as a possible origin for the multiferroicity and the giant magnetoelectric coupling effect near room temperature.⁹ However, the growth mechanism of BKFO nanostructures is still unclear and the 190 °C hydrothermal fabrication of BKFO in an earlier report requires a specialized laboratorial autoclave as the reaction vessel.⁹ Thus, this material cannot be synthesized on a large scale through the previous preparation method.

As we know, nanomaterials are fundamental to modern science and technology, and controllable fabrication of nanocrystals is an important research direction in the field of nanotechnology.^{11–17} Nanostructures with tailored geometries exhibit unique shape-dependent phenomena and subsequent utilization of them as building blocks for the fabrication of nanodevices is of significant interest.¹² Mastery over the shape and morphology of a nanocrystal enables control of its properties and enhancement of its applicability.¹⁷ For example, the magnetic behaviors of Ni,¹⁸ $\alpha\text{-Fe}_2\text{O}_3$,¹⁹ and Fe_3O_4 ²⁰ nanostructures are closely related to their morphologies and the corresponding microstructures. Moreover, strong size-dependent magnetic properties have been found in multiferroic BiFeO_3 nanoparticles,²¹ in which both spin cluster glass behavior and the exchange bias effect are observed,²² indicating a quite different magnetic structure for BiFeO_3 nanocrystals from the bulk material.²³ Therefore, in magnetic and multiferroic systems, the size and morphology of the nanomaterials have a great effect on the magnetic properties but how to fabricate $\text{Bi}_{4.2}\text{K}_{0.8}\text{Fe}_2\text{O}_{9+\delta}$ nanostructures with various morphologies and how the different microstructures affect the magnetic properties of BKFO remain to be addressed. The present study focuses on the morphology control of the BKFO nanostructures as well as its effects on the magnetic properties. Importantly, a facile one-pot synthesis approach to fabricate urchin-like BKFO architectural structures on a large scale is found.

2. Experimental procedure

Analytical grade $\text{Bi}(\text{NO}_3)_3 \cdot 5\text{H}_2\text{O}$, $\text{Fe}(\text{NO}_3)_3 \cdot 9\text{H}_2\text{O}$, KOH and nitric acid were used without further purification. A typical procedure for the synthesis of $\text{Bi}_{4.2}\text{K}_{0.8}\text{Fe}_2\text{O}_9$ nanocrystals

Hefei National Laboratory for Physical Sciences at Microscale, Department of Physics, CAS Key Lab Mat Energy Convers, University of Science and Technology of China, Hefei 230026, PR China. E-mail: lixg@ustc.edu.cn

† Electronic supplementary information (ESI) available. See DOI: 10.1039/c3ce41464g

is as follows: 0.485 g (1 mmol) of $\text{Bi}(\text{NO}_3)_3 \cdot 5\text{H}_2\text{O}$, 0.192 g (0.475 mmol) of $\text{Fe}(\text{NO}_3)_3 \cdot 9\text{H}_2\text{O}$ and 200 μL of concentrated nitric acid were dissolved in deionized (DI) water and the volume of the solution (hereafter called the pre-solution) was kept to 5 mL by adding an appropriate amount of DI water. Then, 15 mL of a KOH solution (16 mol L^{-1}) was prepared and the pre-solution was dropped into the KOH solution under magnetic stirring. After vigorous stirring for 30 minutes, a blood-red suspension solution was formed and was then transferred to a stainless steel Teflon-lined autoclave of 25 mL capacity. The autoclave was heated and maintained at different hydrothermal temperatures for 60 minutes. It is notable that when the hydrothermal temperature is less than 100 $^{\circ}\text{C}$, the autoclave does not need to be used and the whole process can react in a beaker of 25 mL capacity. Finally, the products were collected by precipitation separation, washed thoroughly with DI water and absolute ethanol, and finally dried at 120 $^{\circ}\text{C}$ in an air atmosphere for further characterization.

The products were characterized by X-ray diffraction (XRD) recorded on a Rigaku D/Max-rA X-ray diffractometer with $\text{Cu}-\text{K}\alpha = 0.15418 \text{ nm}$. Field emission scanning electron microscopes (FESEM, FEI Sirion and JEOL-6700) were used to observe the morphologies and analyze the elemental compositions of the as-grown samples. An ultra-thin gold film (about 2 nm) was deposited to improve the FESEM image quality. The microstructure of the products was investigated by high-resolution transmission electron microscope (HRTEM) images and selected area electron diffraction (SAED) patterns recorded on an aberration-corrected transmission electron microscope (JEOL JEM-ARM200F). The magnetic properties of the samples were determined with a superconducting quantum interference device vibrating sample magnetometer (Quantum Design SQUID-VSM).

3. Results and discussion

Fig. 1 illustrates the effects of the different KOH solution temperatures, T_{KOH} (20 $^{\circ}\text{C}$, 50 $^{\circ}\text{C}$ and 90 $^{\circ}\text{C}$), for the co-precipitation processes on the morphologies of the $\text{Bi}_{4.2}\text{K}_{0.8}\text{Fe}_2\text{O}_{9+\delta}$ nanostructures, and the hydrothermal temperature (T_{HT}) is 180 $^{\circ}\text{C}$ for all these three samples. In order to maintain pristine morphologies, the hydrothermal products naturally dispersed in absolute alcohol without ultrasonic or centrifugation treatments are dropped onto copper wafers for characterization by field-emission scanning electron microscope (FESEM). Fig. 1a shows the as-prepared products for $T_{\text{KOH}} = 20^{\circ}\text{C}$ and the inset of Fig. 1a is the low magnification view. The products are dispersible nanobelts with an average width of 200 nm and most of the nanobelts have a length longer than 10 μm though some nanobelt lengths are over 50 μm . For $T_{\text{KOH}} = 50^{\circ}\text{C}$, the nanobelts are no longer dispersible, as shown in Fig. 1b. In this condition, the nanobelts self-assemble into sphere-shaped haystacks and the nanobelt branches are very flexible, the average length of which is 10 μm while the width is around 200 nm. For the case of $T_{\text{KOH}} = 90^{\circ}\text{C}$, the final products become floriated micronanostructures with large belt branches whose average width is about 5 μm (see Fig. 1c). For this relatively high

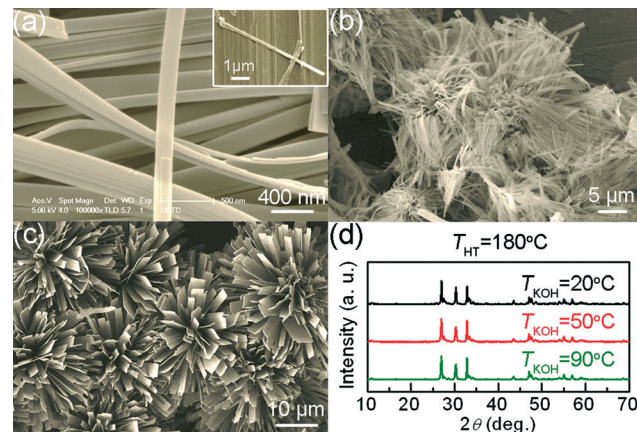


Fig. 1 FESEM images of the $\text{Bi}_{4.2}\text{K}_{0.8}\text{Fe}_2\text{O}_{9+\delta}$ nanostructures obtained at $T_{\text{KOH}} = 20^{\circ}\text{C}$ (a), 50 $^{\circ}\text{C}$ (b) and 90 $^{\circ}\text{C}$ (c), respectively, and all the samples are finally fabricated at $T_{\text{HT}} = 180^{\circ}\text{C}$. The inset of (a) is a panoramic view for a single nanobelt. (d) The corresponding XRD patterns.

KOH solution temperature, the co-precipitation reacts violently and the process is a little hard to control. Fig. 1d shows the X-ray diffraction (XRD) patterns of the above three products synthesized at different T_{KOH} . Although these three samples have different morphologies, the diffraction peaks of them could be indexed to $\text{Bi}_{4.2}\text{K}_{0.8}\text{Fe}_2\text{O}_{9+\delta}$ very well.⁹

Fig. 2 shows the hydrothermal temperature, T_{HT} , dependent morphologies of the products with a fixed $T_{\text{KOH}} = 50^{\circ}\text{C}$ for the co-precipitation step. For $T_{\text{HT}} = 70^{\circ}\text{C}$, the products are hierarchical microspheres with very short nanobelt branches, as shown in Fig. 2a, and the corresponding XRD pattern in Fig. 2d reveals the main diffraction peaks of BKFO already appear although strong monoclinic Bi_2O_3 (120) and (121) diffraction peaks can also be detected. For $T_{\text{HT}} = 90^{\circ}\text{C}$, the products still have spheroidal morphology but the length of the nanobelt branches increases to 1–2 μm (see Fig. 2b) and thus the products look like urchins. Meanwhile, the corresponding

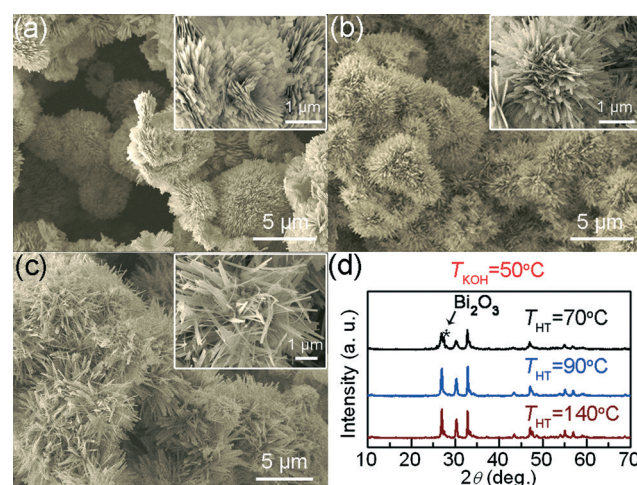


Fig. 2 FESEM images of the products obtained at $T_{\text{KOH}} = 50^{\circ}\text{C}$ and $T_{\text{HT}} = 70^{\circ}\text{C}$ (a), 90 $^{\circ}\text{C}$ (b), and 140 $^{\circ}\text{C}$ (c), respectively. The insets of (a), (b) and (c) are the enlarged views. (d) The corresponding XRD patterns.

XRD patterns show that the Bi_2O_3 peaks actually vanish and the products completely tune into the BKFO phase (see Fig. 2d and Fig. S1, ESI[†]). As T_{HT} rises to 140 °C, the nanobelt branches increase to about 4 μm and the spheroidal contours become blurry because of the crooked nanobelt branches (see Fig. 2c). As shown in Fig. 2d, it is very interesting that the products obtained at $T_{\text{KOH}} = 50$ °C and $T_{\text{HT}} \geq 90$ °C have already transformed to the goal phase despite the fact that BKFO possesses a very complex crystal structure comprised of four elements. Such a low phase formation temperature can be attributed to the co-precipitation reaction process between the acidic pre-solutions and the hot concentrated alkaline solutions, which may provide extra energy for the rapid phase formation. However, the explicit phase formation process should be complicated and difficult to capture by the present experimental results, which needs further investigation.

The microstructure for the urchin-like BKFO nanostructures fabricated at $T_{\text{KOH}} = 50$ °C and $T_{\text{HT}} = 90$ °C is presented in Fig. 3. Fig. 3a is the TEM image for a typical urchin-like nanostructure and Fig. 3b presents the corresponding energy-dispersive X-ray (EDX) elemental maps. One can see that all the related ions are uniformly distributed in the sample and through the quantitative EDX spectrum analyses, the average atom ratio is $\text{Bi}:\text{K}:\text{Fe} = 4.2:0.8:2$. Fig. 3c is the [001] zone axis SAED pattern of a single nanobelt stripped from an urchin shown in the inset of Fig. 3d, and a modulated structural feature can be detected through the superlattice diffraction spot marked using a white arrow, indicating a commensurately modulated structure with 4 times the periodicity of the subcell lattice parameter b . Fig. 3d is the corresponding HRTEM image and the 4 times superstructure along the b -axis can be observed as well. One can see that the modulated structure leads the anisotropy of the a -axis and b -axis in the BKFO crystal, possibly proving an essential origination for the growth direction of the nanobelts along the a -axis.

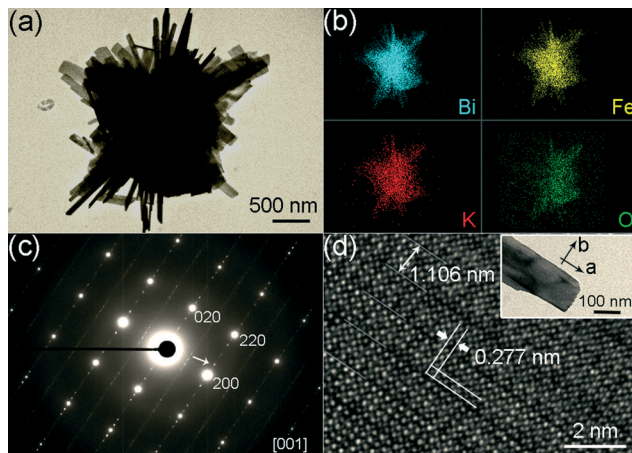


Fig. 3 (a) Typical TEM image and (b) EDX elemental maps of an urchin-like $\text{Bi}_{4.2}\text{K}_{0.8}\text{Fe}_2\text{O}_{9+\delta}$ nanostructure obtained at $T_{\text{KOH}} = 50$ °C and $T_{\text{HT}} = 90$ °C. (c) SAED pattern and (d) HRTEM image of a single nanobelt separated from the urchin-like samples as shown in the inset of (d).

On further increasing T_{HT} to 210 °C ($T_{\text{KOH}} = 50$ °C), the BKFO phase still remains (see Fig. S2 and S3, ESI[†]) but for $T_{\text{HT}} = 220$ °C, the result is quite different, as shown in Fig. 4. Fig. 4a is the FESEM image of the products and two kinds of cubes with different surface roughness can be observed and the corresponding XRD pattern is shown in Fig. 4d. From the diffraction spectrum, two main phases can be indexed which are BiFeO_3 (JCPDS card No. 82-1254) and Bi_2O_3 (JCPDS card No. 76-1730). Based on the EDX spectrum analyses shown in the insets of Fig. 4b and c, those with rougher surfaces are BiFeO_3 (see Fig. 4b) and the others are Bi_2O_3 (Fig. 4c). In an earlier study, it has been found that BKFO nanobelts are unstable in an atmosphere above 450 °C, at which temperature the nanobelts begin breaking down into BiFeO_3 and $\text{Bi}_2\text{O}_3(\text{KBiO}_2)_x$.⁹

Fig. 5 illustrates the morphology-evolutions of the $\text{Bi}_{4.2}\text{K}_{0.8}\text{Fe}_2\text{O}_{9+\delta}$ samples fabricated at different T_{KOH} and T_{HT} . The intermediate precipitates, which do not undergo a final hydrothermal treatment, are obtained by dropping the pre-solution into the KOH solution with $T_{\text{KOH}} = 20$ °C, 50 °C and 90 °C and are collected and examined by FESEM, as shown in Fig. 5a–c. For the precipitates obtained at $T_{\text{KOH}} = 20$ °C, one can see that only nanosized particles have been formed and the size of the particles is not recognizable under a magnification of 80 000× (Fig. 5a). In this case, the products can turn into BKFO nanobelts only when the intermediates are hydro-heated to 180 °C in the autoclave (Fig. 5d and f). On the other hand, the intermediate precipitates for $T_{\text{KOH}} = 50$ °C are microspheres composed of dense nanosheets (Fig. 5b), while those for $T_{\text{KOH}} = 90$ °C are hierarchical microstructures with relatively big and sparse wafers (Fig. 5c). For $T_{\text{KOH}} = 50$ °C, a following $T_{\text{HT}} = 90$ °C for the hydrothermal step can already transform the products into the goal BKFO phase (Fig. 5e). With increasing T_{HT} , the hierarchical microspheres are gradually corroded and the nanobelt petals grow longer until $T_{\text{HT}} = 220$ °C, when the products transform into BiFeO_3 and Bi_2O_3 (Fig. 5i). However, for $T_{\text{KOH}} = 90$ °C,

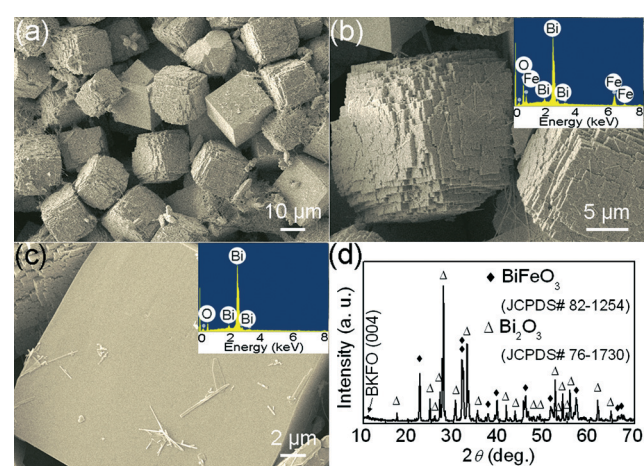


Fig. 4 (a) Low- and (b, c) high-magnification FESEM images of the 220 °C hydrothermal products composed of BiFeO_3 and Bi_2O_3 cubes. The insets of (b) and (c) show the EDX spectra of the cubes with rough and smooth surfaces, respectively. (d) The corresponding XRD pattern of the products.

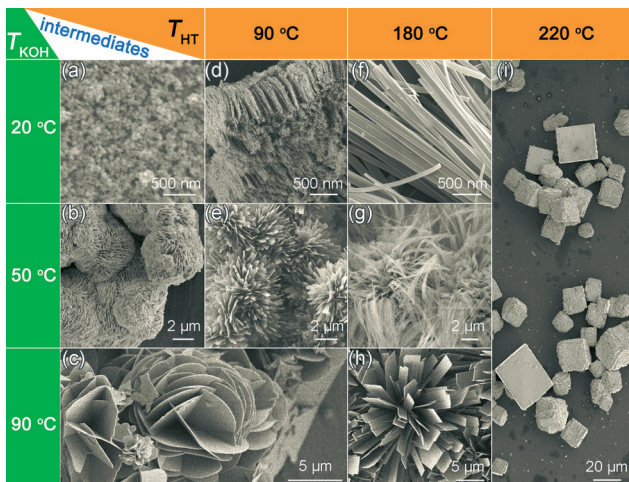


Fig. 5 The morphology-evolution process of the products obtained at different T_{KOH} and T_{HT} . (a–c) FESEM images of the intermediate precipitates, which do not undergo a second step hydrothermal treatment. (d–i) FESEM images of the final products.

as the co-precipitation reaction is violent, the wafers in the microspheres are thicker than those obtained at $T_{\text{KOH}} = 50^\circ\text{C}$, which may cause them to be eroded, so the final hydrothermal products at 180°C have rather large and straight branches (Fig. 5h). Above all, the distinct intermediate precipitates can lead to different morphologies for the final hydrothermal products and a proper KOH solution temperature greatly promotes the crystallinity of the BKFO micronanocrystals. It should be pointed out that for the hydrothermal condition $T_{\text{HT}} < 100^\circ\text{C}$, the whole reaction takes place in a normal beaker and the autoclave is not needed. So the urchin-like BKFO nanostructures can be fabricated on a large scale *via* a very simple method, which is beneficial for industrial production.

Fig. 6 shows the FESEM images of the cross-sections of the $\text{Bi}_{4.2}\text{K}_{0.8}\text{Fe}_2\text{O}_{9+\delta}$ nanostructures fabricated at $T_{\text{KOH}} = 50^\circ\text{C}$ and different T_{HT} , from which an important growth process can be captured. For the cross-section of the products fabricated at $T_{\text{HT}} = 90^\circ\text{C}$, as presented in Fig. 6a, it is observed that the urchin-like BKFO nanostructures can be divided into two parts: the inside cores and the outside nanobelt branches. The inside cores are about $5\text{ }\mu\text{m}$ in diameter and composed of numerous elongated particles, which should be the BKFO phase as no impurity is detected by the XRD in the products (see Fig. 2d and Fig. S1, ESI[†]). These elongated particles are aligned in lines along with different outside nanobelt branches and this kind of highly regular arrangement implies the growth process of the outside nanobelt branches might contain an oriented attachment feature.^{24–29} Fig. 6c and d show the cross-sections for the products obtained at $T_{\text{HT}} = 180^\circ\text{C}$ at different magnifications. It is notable that the diameter of the cores in the BKFO nanostructures decreases to $2\text{ }\mu\text{m}$ and many obvious cavities appear, implying the cores are gradually consumed as the outside nanobelt branches grow longer. When the T_{HT} is 210°C , as shown in Fig. 6e and Fig. S3, ESI[†] only a few small cores can be found (about $1\text{ }\mu\text{m}$ in diameter) and they are too loose to connect to the outside nanobelt

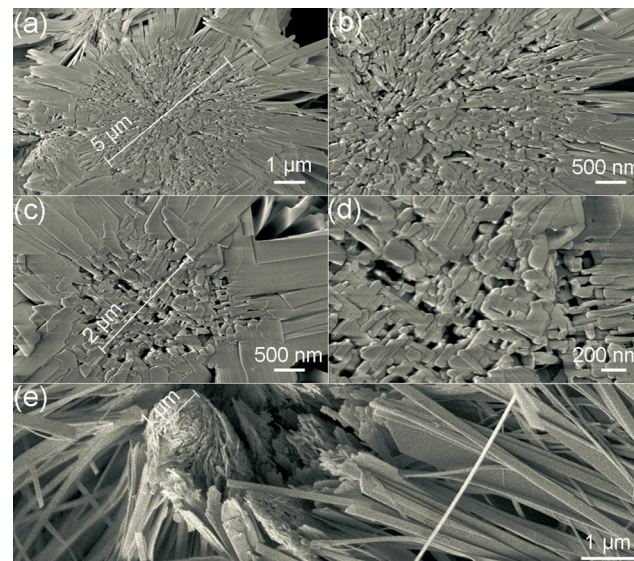


Fig. 6 FESEM images of the cross-section of the $\text{Bi}_{4.2}\text{K}_{0.8}\text{Fe}_2\text{O}_{9+\delta}$ nanostructures obtained at $T_{\text{KOH}} = 50^\circ\text{C}$ and $T_{\text{HT}} = 90^\circ\text{C}$ (a, b), 180°C (c, d), and 210°C (e).

branches, so the surrounding branches fall from the cores and become dispersed nanobelts.

From the results mentioned above, possible growth mechanisms of the BKFO nanostructures are proposed, as schematically illustrated in Fig. 7. The growth of the BKFO nanostructures can be fabricated through the following two different approaches. 1) The first one is common hydrothermal growth for oxide nanobelts.^{30–32} In this way, ultra-fine particle precursors are formed by a co-precipitation reaction in a normal-temperature KOH solution ($\sim 20^\circ\text{C}$) and then a suitable hydrothermal temperature and internal high pressure arouses the nucleation and growth of BKFO crystals from the precursors *via* a dissolution-recrystallization process.^{33–35} At last, the BKFO nanobelts are obtained with (100) oriented growth due to the highly anisotropic and intrinsic nature of the BKFO crystals.⁹ 2) For the second one, the hierarchical microsphere precursors are formed by co-precipitation in a high-temperature KOH solution ($\sim 50^\circ\text{C}$). The hierarchical microspheres may have high

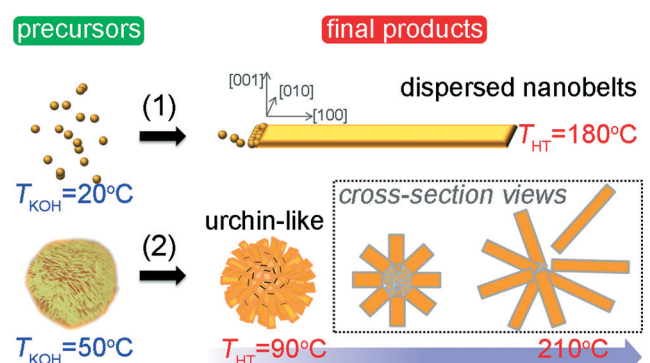


Fig. 7 Schematic illustration of the formation process for the $\text{Bi}_{4.2}\text{K}_{0.8}\text{Fe}_2\text{O}_{9+\delta}$ nanostructures.

chemical reactivity and can be easily converted into the BKFO phase by a further hydrothermal reaction at 90 °C for 60 minutes under an ordinary pressure. In addition, the cross-section views of the urchin-like nanostructures indicate an oriented attachment process may also be involved in helping the elongated BKFO particles in the cores gradually evolve into the nanobel branches (see more related FESEM images in Fig. S4, ESI†). Finally, the depletion of the cores at $T_{HT} = 210$ °C gives rise to the abscission of the outside branches and dispersed BKFO nanobelts are obtained.

It is of interest to investigate the magnetic behaviors of the $\text{Bi}_{4.2}\text{K}_{0.8}\text{Fe}_2\text{O}_{9+\delta}$ samples with different morphologies. Fig. 8a shows the magnetic hysteresis loops at 300 K for the samples obtained at different T_{KOH} and T_{HT} . One can see that the curves almost coincide with each other for the samples obtained at a T_{HT} value of 180 °C and different T_{KOH} values. In contrast, for the samples with fixed $T_{KOH} = 50$ °C and different T_{HT} , the magnetizations increase as T_{HT} decreases. Similar results have also been observed from the M - H curves measured at 10 K, besides a relatively strong ferromagnetism (see Fig. S5, ESI†). Hence, the low-temperature-fabricated urchin-like BKFO nanostructures can not only be obtained *via* a more facile way but also have enhanced magnetic properties. Fig. 8b and c show the temperature dependencies of the zero field cooled (ZFC) and field cooled (FC) magnetizations at 100 Oe for the samples obtained at $T_{HT} = 180$ °C and $T_{HT} = 90$ °C, respectively ($T_{KOH} = 50$ °C). All the ZFC curves have an obvious separation from the corresponding FC curves below the freezing temperatures, T_f (near the peak temperature of the ZFC curves).²² The results suggest that there may be a spin-glass-like behavior at low temperatures in the system. With the increase of the hydrothermal temperature, the separation between the ZFC and FC curves gradually becomes inconspicuous. Therefore, the hydrothermal temperature has an important effect on the magnetic behavior of the samples, while T_{KOH} is not so critical for this. The most probable origin for the enhanced magnetism of the samples synthesized at a

relatively low hydrothermal temperature is due to the cores, which are composed of numerous elongated BKFO nanoparticles, as shown in Fig. 6. The magnetic ground state of BKFO is anti-ferromagnetic⁹ but the size effect of the elongated particles in the cores can partly destroy antiferromagnetic ordering and more uncompensated moments appear due to the large specific surface, where spin-clusters could form naturally.²¹ As the hydrothermal temperature increases, the outside nanobel branches grow longer and the volume fraction of the cores decreases. As a result, the magnetizations of such BKFO nanostructures get closer to that of the pure BFKO nanobelts for a higher T_{HT} . Moreover, the special cores with the stronger magnetizations may play an important role for the self-assembly of the inside elongated particles as well as the whole urchin-like nanostructures.³⁶⁻³⁸

In order to characterize the dynamics of the spin-glass-like behavior, the temperature dependencies of the real part, χ' , and the imaginary part, χ'' , of the ac susceptibilities for the different samples are measured with an ac magnetic field of 3 Oe at different frequencies (f). Fig. 9a presents the results for the sample obtained at $T_{KOH} = 50$ °C, $T_{HT} = 180$ °C as an example. The peak of $\chi'(T)$ shifts towards higher temperatures as the frequency increases, which can be fitted to a critical power law,³⁹

$$\tau = \tau_0 (T_f/T_g - 1)^{-z\nu}, \quad (1)$$

where the relaxation time $\tau = 1/2\pi f$, describing the dynamical fluctuation time scale, τ_0 is the relaxation time constant, T_g is the spin-cluster glass transition temperature, and $z\nu$ is the dynamic critical exponent. As shown in Fig. 9b, the best fit of the $\tau(T_f)$ data to eqn (1) yields $\tau_0 \approx 7.49 \times 10^{-8}$ s, $T_g = 25.6 \pm 0.8$ K and $z\nu = 9.8 \pm 1.6$, and these values are close to those reported for spin-glass and cluster-glass systems.^{22,40,41} Fig. 9c shows the fitting curve for the urchin-like sample obtained at $T_{KOH} = 50$ °C, $T_{HT} = 90$ °C, and the dynamical parameters are calculated to be $\tau_0 \approx 1.78 \times 10^{-7}$ s, $T_g = 25.2 \pm 1.6$ K and

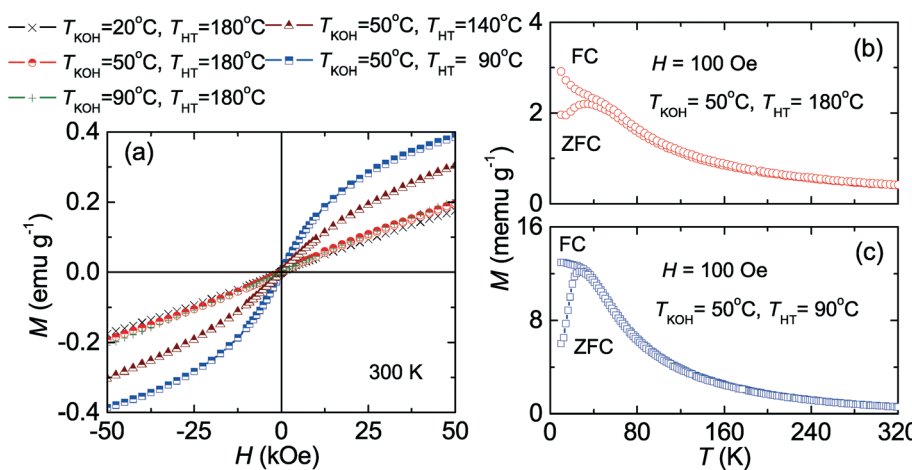


Fig. 8 (a) M - H curves measured at 300 K for the samples fabricated at different conditions. (b, c) Temperature dependencies of the ZFC and FC magnetizations at 100 Oe for the samples obtained at (b) $T_{KOH} = 50$ °C, $T_{HT} = 180$ °C and (c) $T_{KOH} = 50$ °C, $T_{HT} = 90$ °C, respectively.

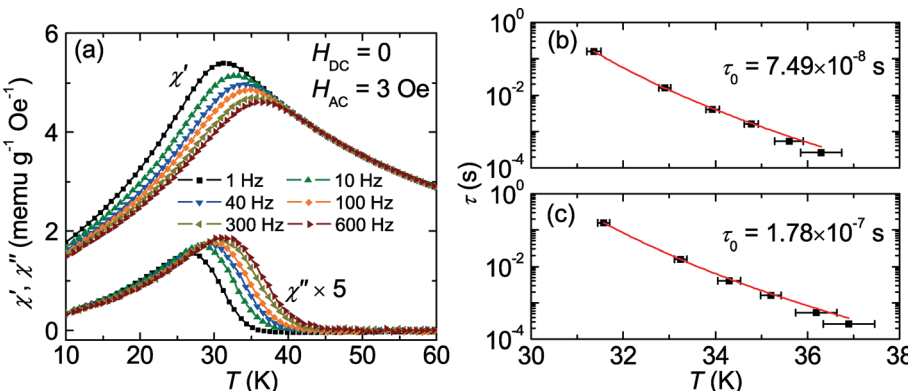


Fig. 9 (a) Temperature dependencies of the real part, χ' , and the imaginary part, χ'' , of the ZFC ac susceptibilities for the $\text{Bi}_{4.2}\text{K}_{0.8}\text{Fe}_2\text{O}_{9+\delta}$ nanostructures ($T_{\text{KOH}} = 50$ °C, $T_{\text{HT}} = 180$ °C) at different frequencies. (b, c) The logarithmic plots of τ versus T and the related best fits to eqn (1) for the samples obtained at (b) $T_{\text{KOH}} = 50$ °C, $T_{\text{HT}} = 180$ °C and (c) $T_{\text{KOH}} = 50$ °C, $T_{\text{HT}} = 90$ °C, respectively.

$z\nu = 9.9 \pm 1.9$. The relatively large τ_0 implies the ferromagnetic-like spin-clusters in the low-temperature-fabricated urchin-like nanostructures are much bigger than those in the samples obtained at $T_{\text{HT}} = 180$ °C, and the big spin-clusters can bring more net moments to enhance the magnetization, as shown in Fig. 8 and 9. Below T_g , the spin-clusters in the nanostructures, contributing additional magnetic moments under the anti-ferromagnetic background of BKFO, are ferromagnetic-like, for instance, the magnetic properties at 10 K, as shown in Fig. S5 and S6, ESI†, while at 300 K, far above T_g , most spin-clusters become paramagnetic due to the thermal agitation (Fig. 8a).⁴² However, even in this case very weak ferromagnetic-like spin-clusters still exist,⁹ which contribute to the relatively large susceptibility, especially in the urchin-like $\text{Bi}_{4.2}\text{K}_{0.8}\text{Fe}_2\text{O}_{9+\delta}$ nanostructures obtained at $T_{\text{KOH}} = 50$ °C, $T_{\text{HT}} = 90$ °C (see Fig. S7, ESI†).

4. Conclusions

In summary, different $\text{Bi}_{4.2}\text{K}_{0.8}\text{Fe}_2\text{O}_{9+\delta}$ nanostructures with controllable morphologies are successfully fabricated by a simple hydrothermal synthesis approach. The reaction temperatures, such as those of the KOH solutions for the co-precipitation step and the hydrothermal reaction, play critical roles in determining the final morphologies of the products. Moreover, the magnetic properties of the multiferroic $\text{Bi}_{4.2}\text{K}_{0.8}\text{Fe}_2\text{O}_{9+\delta}$ nanostructures with different morphologies exhibit spin-glass-like behavior. A facile one-pot synthesis route for fabricating the urchin-like $\text{Bi}_{4.2}\text{K}_{0.8}\text{Fe}_2\text{O}_{9+\delta}$ nanostructures on a large scale with a higher magnetization is developed. These findings may be useful for practical applications.

Acknowledgements

This work is supported by the National Natural Science Foundation of China, the National Basic Research Program of China (Contract No. 2012CB922003, 2011CBA00102 and 2009CB929502) and the Fundamental Research Funds for the Central Universities (Contract No. WK2060140009).

References

- M. Fiebig, *J. Phys. D: Appl. Phys.*, 2005, **38**, R123–R152.
- N. A. Spaldin and M. Fiebig, *Science*, 2005, **309**, 391–392.
- S. W. Cheong and M. Mostovoy, *Nat. Mater.*, 2007, **6**, 13–20.
- K. F. Wang, J. M. Liu and Z. F. Ren, *Adv. Phys.*, 2009, **58**, 321–448.
- J. Ma, J. M. Hu, Z. Li and C. W. Nan, *Adv. Mater.*, 2011, **23**, 1062–1087.
- J. Wang, J. B. Neaton, H. Zheng, V. Nagarajan, S. B. Ogale, B. Liu, D. Viehland, V. Vaithyanathan, D. G. Schlom, U. V. Waghmare, N. A. Spaldin, K. M. Rabe, M. Wuttig and R. Ramesh, *Science*, 2003, **299**, 1719–1722.
- Y. Kitagawa, Y. Hiraoka, T. Honda, T. Ishikura, H. Nakamura and T. Kimura, *Nat. Mater.*, 2010, **9**, 797–802.
- G. H. Zhang, H. Wu, G. B. Li, Q. Z. Huang, C. Y. Yang, F. Q. Huang, F. H. Liao and J. H. Lin, *Sci. Rep.*, 2013, **3**, 1265.
- S. N. Dong, Y. P. Yao, J. Q. Li, Y. J. Song, Y. K. Liu and X. G. Li, *Sci. Rep.*, 2013, **3**, 1245.
- Y. Le Page, W. R. McKinnon, J. M. Tarascon and P. Barboux, *Phys. Rev. B*, 1989, **40**, 6810.
- C. Burda, X. B. Chen, R. Narayanan and M. A. El-Sayed, *Chem. Rev.*, 2005, **105**, 1025–1102.
- Y. W. Jun, J. S. Choi and J. Cheon, *Angew. Chem., Int. Ed.*, 2006, **45**, 3414–3439.
- P. D. Cozzoli, T. Pellegrino and L. Manna, *Chem. Soc. Rev.*, 2006, **35**, 1195–1208.
- J. Park, J. Joo, S. G. Kwon, Y. Jang and T. Hyeon, *Angew. Chem., Int. Ed.*, 2007, **46**, 4630–4660.
- A. R. Tao, S. Habas and P. D. Yang, *Small*, 2008, **4**, 310–325.
- M. Grzelczak, J. Perez-Juste, P. Mulvaney and L. M. Liz-Marzan, *Chem. Soc. Rev.*, 2008, **37**, 1783–1791.
- Y. N. Xia, Y. J. Xiong, B. Lim and S. E. Skrabalak, *Angew. Chem., Int. Ed.*, 2009, **48**, 60–103.
- G. Q. Zhang, T. Zhang, X. L. Lu, W. Wang, J. F. Qu and X. G. Li, *J. Phys. Chem. C*, 2007, **111**, 12663–12668.
- D. Jagadeesan, U. Mansoori, P. Mandal, A. Sundaresan and M. Eswaramoorthy, *Angew. Chem., Int. Ed.*, 2008, **47**, 7685–7688.

- 20 L. J. Zhao, H. J. Zhang, Y. Xing, S. Y. Song, S. Y. Yu, W. D. Shi, X. M. Guo, H. H. Yang, Y. Q. Le and F. Cao, *Chem. Mater.*, 2008, **20**, 198–204.
- 21 T. J. Park, G. C. Papaefthymiou, A. J. Viescas, A. R. Moodenbaugh and S. S. Wong, *Nano Lett.*, 2007, **7**, 766–772.
- 22 S. N. Dong, Y. P. Yao, Y. Hou, Y. K. Liu, Y. Tang and X. G. Li, *Nanotechnology*, 2011, **22**, 385701.
- 23 D. Lebeugle, D. Colson, A. Forget, M. Viret, P. Bonville, J. F. Marucco and S. Fusil, *Phys. Rev. B: Condens. Matter Mater. Phys.*, 2007, **76**, 024116.
- 24 N. Pradhan, H. F. Xu and X. G. Peng, *Nano Lett.*, 2006, **6**, 720–724.
- 25 A. Halder and N. Ravishankar, *Adv. Mater.*, 2007, **19**, 1854–1858.
- 26 K. T. Yong, Y. Sahoo, H. Zeng, M. T. Swihart, J. R. Minter and P. N. Prasad, *Chem. Mater.*, 2007, **19**, 4108–4110.
- 27 Q. Zhang, S. J. Liu and S. H. Yu, *J. Mater. Chem.*, 2009, **19**, 191–207.
- 28 H. Y. Liang, H. G. Zhao, D. Rossouw, W. Z. Wang, H. X. Xu, G. A. Botton and D. L. Ma, *Chem. Mater.*, 2012, **24**, 2339–2346.
- 29 D. S. Li, M. H. Nielsen, J. R. I. Lee, C. Frandsen, J. F. Banfield and J. J. De Yoreo, *Science*, 2012, **336**, 1014–1018.
- 30 R. H. Ma, Y. Bando, L. Q. Zhang and T. Sasaki, *Adv. Mater.*, 2004, **16**, 918–922.
- 31 J. F. Liu, Q. H. Li, T. H. Wang, D. P. Yu and Y. D. Li, *Angew. Chem., Int. Ed.*, 2004, **43**, 5048–5052.
- 32 R. Q. Song, A. W. Xu and S. H. Yu, *J. Am. Chem. Soc.*, 2007, **129**, 4152–4153.
- 33 G. C. Xi, K. Xiong, Q. B. Zhao, R. Zhang, H. B. Zhang and Y. T. Qian, *Cryst. Growth Des.*, 2006, **6**, 577–582.
- 34 X. L. Hu, Y. Masuda, T. Ohji and K. Kato, *Cryst. Growth Des.*, 2010, **10**, 626–631.
- 35 K. M. O. Jensen, M. Christensen, C. Tyrsted, M. Bremholm and B. B. Iversen, *Cryst. Growth Des.*, 2011, **11**, 753–758.
- 36 B. Y. Kim, I. B. Shim, O. L. A. Monti and J. Pyun, *Chem. Commun.*, 2011, **47**, 890–892.
- 37 R. J. Hickey, A. S. Haynes, J. M. Kikkawa and S. J. Park, *J. Am. Chem. Soc.*, 2011, **133**, 1517–1525.
- 38 J. Yan, M. Bloom, S. C. Bae, E. Luijten and S. Granick, *Nature*, 2012, **491**, 578–582.
- 39 P. C. Hohenberg and B. I. Halperin, *Rev. Mod. Phys.*, 1977, **49**, 435.
- 40 X. H. Huang, J. F. Ding, Z. L. Jiang, Y. W. Yin, Q. X. Yu and X. G. Li, *J. Appl. Phys.*, 2009, **106**, 083904.
- 41 S. Sabyasachi, M. Patra, S. Majumdar, S. Giri, S. Das, V. S. Amaral, O. Iglesias, W. Borghols and T. Chatterji, *Phys. Rev. B: Condens. Matter Mater. Phys.*, 2012, **86**, 104416.
- 42 S. Bedanta and W. Kleemann, *J. Phys. D: Appl. Phys.*, 2009, **42**, 013001.